Reflectivity Study of Microwave Blackbody Target

Dazhen Gu, *Senior Member, IEEE*, Derek Houtz, James Randa, *Senior Member, IEEE*, and David K. Walker, *Senior Member, IEEE*

***Abstract*—We report on the characterization of blackbody target reflections as part of the recent progress on the development of brightness temperature standards for microwave remote sensing at the National Institute of Standards and Technology. The very low reflections from the blackbody targets used in airborne or satellite remote sensing systems present challenges on how to extract reflection coefficients from the measurements. A full calibration technique is developed for this study by the use of a flat aluminum plate used as a known standard in combination with measurements of the empty anechoic chamber. The theoretical basis and measurement procedures, along with the uncertainty analysis, are presented. Calibration results validate the method by showing its independence from measurement hardware and conditions. A comparison between the theoretical prediction of reflection coefficients of a free-standing dielectric slab with well-documented physical parameters and the de-embedded reflection coefficients from experiments confirms good calibration accuracy. The specific blackbody target used in this paper shows well-matched properties with a power reflectivity below −40 dB over the entire measurement band (18 to 26 GHz).**

***Index Terms*—Anechoic chamber, blackbody target, free-space calibration, reflection measurement, uncertainty analysis.**

I. Introduction

MICROWAVE sounding and imaging data from airborne and satellite instruments are one of the key components for global temperature observation [1], [2], numerical weather prediction [3], and soil moisture [4] and ocean salinity [5] detection. Many passive microwave radiometric systems equipped on airborne and satellite units have been developed or are under development worldwide. To name a few, the Advanced Microwave Sounding Unit [6] and the Advanced Technology Microwave Sounder [7] in the U.S., the FengYun system [8] in China, and the European Organisation for the Exploitation of Meteorological Satellites Polar System [9] in Europe. Efforts have been driven by the need for monitoring agricultural and environmental (such as land and water) resources and, most recently, climate change.

Manuscript received November 24. 2010; revised February 14, 2011; accepted March 3, 2011. Date of current version August 26, 2011.

D. Gu and D. K. Walker are with the Electromagnetics Division, National Institute of Standards and Technology, Boulder, CO 80305 USA (e-mail: dazhen.gu@nist.gov; david.walker@nist.gov).

D. Houtz is with the Electromagnetics Division, National Institute of Standards and Technology, Boulder, CO 80305 USA, and also with the Department of Aerospace Engineering Sciences, University of Colorado, Boulder, CO 80309 USA (e-mail: derek.houtz@nist.gov).

J. Randa is with the Electromagnetics Division, National Institute of Standards and Technology, Boulder, CO 80305 USA, and also with the Department of Physics, University of Colorado, Boulder, CO 80309 USA (e-mail: james.randa@nist.gov).

Digital Object Identifier 10.1109/TGRS.2011.2125975

Although they may be constructed in different ways or carry out different missions, most passive microwave radiometers include a blackbody radiator, often called a brightness standard, as a reference. Calibrated brightness temperature standards at microwave frequencies ensure the accuracy of the microwave data, particularly for global warming studies when the absolute value, instead of the relative value, of the Earth temperatures is required. However, national standards for microwave brightness temperature are yet to be established. Many such standards are realized in the form of heated or cooled targets, but none is currently maintained by a National Measurement Institute. Approximation has been made in current arts in which the brightness temperature of the target is estimated by using the physical temperature measured with calibrated thermal sensors. This approach has been helpful in the monitoring of relative temperature changes in short-term weather forecast, but improvement is needed for the long-term assessment of climate drift.

We are developing microwave brightness temperature standards at the National Institute of Standards and Technology (NIST). The project involves the full characterization of calibration targets by the use of standard radiometers traceable to primary noise standards [10]. In addition to the brightness temperature measurements, we are also investigating the reflection of the calibration targets as a complementary study. The importance of the reflection measurements arises from its direct link to the emissivity (based on Kirchhoff's radiation law), a parameter that quantifies how close the target is to an ideal blackbody. Most radiometric systems desire low reflections from calibration targets in the operational frequency range. The approximation used to estimate the brightness temperature (T_B) by the physical temperature (T_{phy}) produces more calibration error as the property of the target deviates from an ideal blackbody. For any object with a perfectly planar and smooth surface, its p-polarized emissivity (e_p) along the view angle θ relates to the reflectivity $(|\mathbf{\Gamma}_p|^2)$ as $e_p(\theta) = 1 - |\mathbf{\Gamma}_p(\theta)|^2$. For nonideal situations, the scattering over the entire hemisphere must be included [11]. As a result, the emissivity is represented by $e_p(\theta) = 1 - r_p(\theta) - s_p(\theta)$, where $r_p(\theta)$ and $s_p(\theta)$ denote the normalized reflected energy coefficient and scattered energy coefficient, respectively. At this preliminary stage, this paper is limited to the reflection from a blackbody by radiation at approximately normal incidence $(\theta = 0)$ in the far field with minimal phase error using a monostatic setup. More comprehensive study requires the investigation of the angular dependence of scattering coefficients with bistatic antennas.

There are a few measurement methods available for the characterization of backscatter properties of objects. Coaxial transmission-line [12] or open-ended coaxial probe [13]

techniques may be used. However, these methods have some disadvantages because of their strict sample preparation requirements and limited frequency band due to the presence of higher order modes. For samples with explicit surface configurations (such as RF absorbers and blackbody targets), free-space contactless measurements are often used. Such measurements can be implemented by the use of common monostatic or bistatic antenna systems or more sophisticated antenna and lens coupling systems [14]. Lenses are used to bundle the electromagnetic (EM) radiation from the antenna, resulting in nearly ideal normal incidence on objects of interest. However, the addition of the different lenses for various frequency bands may make the system more cumbersome. In our investigation of blackbody targets, we have been using standard horn antennas without lenses.

Accurate measurements of reflection coefficients in a noncontact mode are challenging. Such measurements are usually performed in an anechoic chamber by the use of an antenna in connection with a calibrated vector network analyzer (VNA). The antenna acts as a free-space transmitter and receiver. The radiated power from the antenna reaching objects of fixed size varies as a function of their separation distance. Such variation is particularly significant in the near-field region, where the calibration targets are located for applications in many airborne or spaceborne instruments. Furthermore, calibration targets are designed to produce negligible reflection in their operation band. The measured quantity associated with the targets' reflection is often near or below the uncertainty of the VNA.

In this paper, we report on a theoretical and experimental study of reflection coefficients of calibration targets in free-space measurements. The theoretical modeling, some solution procedures, uncertainty analysis, and verification methods are outlined in Section II. Section III details the measurement setup and conditions. Experimental results are presented in Section IV. The discussion and conclusion are given at the end.

II. Theory

A de-embedding process is required in order to extract the free-space reflection coefficient of an object under test (OUT) from the background reflections from other objects. Direct measurements of reflection coefficients are usually at this reference plane where the antenna flange is connected to the coax-to-waveguide adapter. Similar to the two-tier calibration technique in the on-wafer environment [15], a one-port calibration is done at the reference plane prior to the free-space measurements (see Fig. 1). Next, a few free-space calibration standards of known reflection coefficients are needed in order to correct the error terms arising from the antenna reflection, free-space path loss, mismatch between free space and the OUT, etc. The problem can be modeled as a two-port network terminated by the OUT [16]. The measured reflection coefficients can be presented by

$$\mathbf{\Gamma}_{\mathrm{meas}} = \mathbf{S}_{11} + \frac{\mathbf{S}_{12}\mathbf{S}_{21}\mathbf{\Gamma}_o}{1 - \mathbf{S}_{22}\mathbf{\Gamma}_o} \tag{1}$$

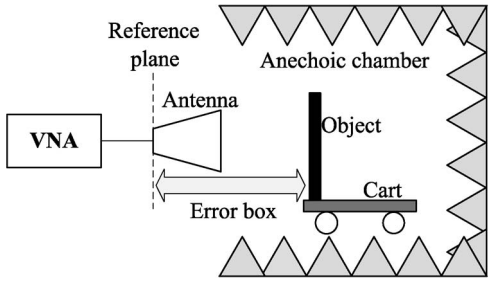

Fig. 1. One-port waveguide calibration is done at the dashed line. The double arrows indicate the error box of the free-space measurements to be solved.

where $\mathbf{\Gamma}_{\mathrm{meas}}$ is the reflection coefficient measured by the VNA; $\mathbf{S}_{11}$, $\mathbf{S}_{12}$, $\mathbf{S}_{21}$, and $\mathbf{S}_{22}$ are scattering parameters of the two-port network to be corrected; and $\mathbf{\Gamma}_o$ is the reflection coefficient of the OUT. To simplify the problem, we revise (1) in a three-error-term format, i.e.,

$$\mathbf{\Gamma}_{\mathrm{meas}} = \mathbf{e}_1 + \frac{\mathbf{e}_2\mathbf{\Gamma}_o}{1 - \mathbf{e}_3\mathbf{\Gamma}_o}. \tag{2}$$

In principle, three different objects with known reflection coefficients are required to calibrate the error terms, which, in turn, allow us to solve any unknown reflection $\mathbf{\Gamma}_o$ from the measurement $\mathbf{\Gamma}_{\mathrm{meas}}$ as

$$\mathbf{\Gamma}_o = \frac{\mathbf{\Gamma}_{\mathrm{meas}} - \mathbf{e}_1}{\mathbf{e}_2 + \mathbf{e}_3(\mathbf{\Gamma}_{\mathrm{meas}} - \mathbf{e}_1)}. \tag{3}$$

This is similar in some ways to previous work [17] in blackbody target characterization. Our present approach employs a more formalized calibration procedure.

A. Ripple Method

Blackbody targets for remote sensing are usually designed to produce very small reflections in the operation frequency range. Therefore, the denominator of the second term on the right side of (2) can be approximated as 1. Equation (2) is then reduced to

$$\mathbf{\Gamma}_{\mathrm{meas}} \approx \mathbf{e}_1 + \mathbf{e}_2\mathbf{\Gamma}_o. \tag{4}$$

The error term $\mathbf{e}_2$ accounts for the fact that the target intercepts only a fraction of the radiated beam. Even if the target was a perfect reflector, only a fraction of the radiated power would be reflected. Physically, the error term $\mathbf{e}_1$ accounts for the reflections that occur even when there is no target present. The principal contribution to $\mathbf{e}_1$ is from the antenna itself and from the mismatch between the antenna and free space. There are also contributions to $\mathbf{e}_1$ from reflections from the chamber walls. $\mathbf{e}_1$ remains almost unchanged once the measurement hardware is set up. Due to the nonnegligible term $\mathbf{e}_2\mathbf{\Gamma}_o$, a standing wave is present between the measurement reference plane and the target. The ripple method is designed to set the target at variable positions along the longitudinal direction while keeping the target aligned with the antenna. $\mathbf{\Gamma}_{\mathrm{meas}}$ is the superposition of the fixed vector $\mathbf{e}_1$ and the rotating vector $\mathbf{e}_2\mathbf{\Gamma}_o$. The magnitude of $\mathbf{\Gamma}_{\mathrm{meas}}$ as a function of the distance shows a ripple-type response; it reaches a maximum when $\mathbf{e}_1$ and $\mathbf{e}_2\mathbf{\Gamma}_o$ are in phase, and it reaches a minimum when they

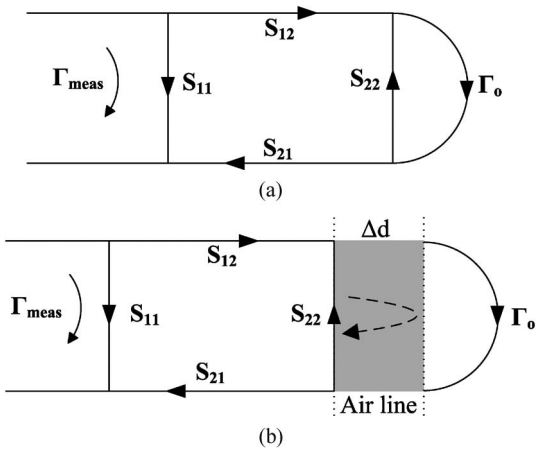

Fig. 2. (a) Error box signal flow graph. (b) Object offset from the original position is equivalent to adding a transmission line in front of objects.

are 180° out of phase. The magnitudes of $\mathbf{e}_1$ and $\mathbf{e}_2\mathbf{\Gamma}_o$ are solved as

$$|\mathbf{e}_1| = \begin{cases} \frac{|\mathbf{\Gamma}_{\text{meas}}|_{\max}+|\mathbf{\Gamma}_{\text{meas}}|_{\min}}{2}, & \text{if } |\mathbf{e}_1| > |\mathbf{e}_2\mathbf{\Gamma}_o|; \\ \frac{|\mathbf{\Gamma}_{\text{meas}}|_{\max}-|\mathbf{\Gamma}_{\text{meas}}|_{\min}}{2}, & \text{if } |\mathbf{e}_1| < |\mathbf{e}_2\mathbf{\Gamma}_o|; \end{cases} \tag{5a}$$

$$|\mathbf{e}_2\mathbf{\Gamma}_o| = \begin{cases} \frac{|\mathbf{\Gamma}_{\text{meas}}|_{\max}-|\mathbf{\Gamma}_{\text{meas}}|_{\min}}{2}, & \text{if } |\mathbf{e}_1| > |\mathbf{e}_2\mathbf{\Gamma}_o|; \\ \frac{|\mathbf{\Gamma}_{\text{meas}}|_{\max}+|\mathbf{\Gamma}_{\text{meas}}|_{\min}}{2}, & \text{if } |\mathbf{e}_1| < |\mathbf{e}_2\mathbf{\Gamma}_o|. \end{cases} \tag{5b}$$

If the magnitude of $\mathbf{e}_2$ is known or can be estimated, (5b) can be used to determine or estimate the magnitude of $\mathbf{\Gamma}_o$ [17]. To extract both the phase and the magnitude of $\mathbf{\Gamma}_o$, it is necessary to determine the complex value of $\mathbf{e}_2$, as will be done in the data analysis in Section IV.

Taking advantage of numerical fitting, we can extend the ripple method to extract the complex value of $\mathbf{e}_2\mathbf{\Gamma}_o$. In a microwave-circuit point of view, we consider the movement of the target from the original spot equivalent to adding a lossless airline offset (see Fig. 2) in front of the target. In other words, $\mathbf{\Gamma}_o$ becomes $\mathbf{\Gamma}_o \exp(-j\beta 2\Delta d)$, where β is the wavenumber and Δd is the separation between the translated position and the starting position. Equation (4) can be reorganized in a matrix format

$$\begin{bmatrix} 1 & 0 & \cos\left(2\beta\Delta d^{(1)}\right) & -\sin\left(2\beta\Delta d^{(1)}\right) \\ 0 & 1 & \sin\left(2\beta\Delta d^{(1)}\right) & \cos\left(2\beta\Delta d^{(1)}\right) \\ \vdots & \vdots & \vdots & \vdots \\ 1 & 0 & \cos\left(2\beta\Delta d^{(n)}\right) & -\sin\left(2\beta\Delta d^{(n)}\right) \\ 0 & 1 & \sin\left(2\beta\Delta d^{(n)}\right) & \cos\left(2\beta\Delta d^{(n)}\right) \end{bmatrix} \cdot \begin{bmatrix} \Re(\mathbf{e}_1) \\ \Im(\mathbf{e}_1) \\ \Re(\mathbf{e}_2\mathbf{\Gamma}_o) \\ \Im(\mathbf{e}_2\mathbf{\Gamma}_o) \end{bmatrix} \approx \begin{bmatrix} \Re\left(\mathbf{\Gamma}_{\text{meas}}^{(1)}\right) \\ \Im\left(\mathbf{\Gamma}_{\text{meas}}^{(1)}\right) \\ \vdots \\ \Re\left(\mathbf{\Gamma}_{\text{meas}}^{(n)}\right) \\ \Im\left(\mathbf{\Gamma}_{\text{meas}}^{(n)}\right) \end{bmatrix} \tag{6}$$

where the number in the superscript corresponds to the position numbers and $\Re$ and $\Im$ refer to real and imaginary parts. Equation (6) can be solved by the use of linear least squares fitting. Although the value is more accurate and in a complex format in comparison to what is obtained from the simple ripple method, the unknown $\mathbf{e}_2$ again disguises the true value of $\mathbf{\Gamma}_o$.

B. Full Calibration Method

In order to solve for all the error terms, different impedance standards of known $\mathbf{\Gamma}_o$'s need to be measured for system calibration purposes. Similar to the one-port waveguide calibration in the guided wave condition, one-port free-space calibration consists of three known standards: a matched load, a short, and an offset short. The matched load usually corresponds to the condition when the antenna is pointed to the sky or, in our case, when the antenna looks at an anechoic chamber without the presence of any test objects. The short is a metal plate of the same shape as the OUT placed at the position where the OUT will be set. A flat aluminum plate is a good approximation to a perfect reflector in the microwave frequency range. The offset short is the same metal plate but located at a different position while keeping the center of the metal plate aligned with the axis of the antenna. In practice, we measure the metal plate reflection at multiple offset positions for the purpose of redundancy. In addition to the phase delay, a loss term is added to the offset reflection to include the change of antenna effective radiation on objects due to the increment of the distance. It is worth emphasizing that the free-space air loss, a conventional meaning of α, is negligible in comparison to the change of the radiation pattern. The addition of the loss term is crucial, particularly in the near-field and midfield ranges, which will be confirmed in our experimental results. Equation (2) can be expanded to solve the error terms as follows:

$$\mathbf{\Gamma}_{\text{meas}}^{\text{chamber}} = \mathbf{e}_1 \tag{7a}$$

$$\mathbf{\Gamma}_{\text{meas}}^{\text{short}} = \mathbf{e}_1 + \frac{\mathbf{e}_2(-1)}{1-\mathbf{e}_3(-1)} \tag{7b}$$

$$\mathbf{\Gamma}_{\text{meas}}^{\text{offset}} = \mathbf{e}_1 + \frac{\mathbf{e}_2\left\{-\exp\left[-(\alpha+j\beta)\cdot 2\Delta d\right]\right\}}{1-\mathbf{e}_3\left\{-\exp\left[-(\alpha+j\beta)\cdot 2\Delta d\right]\right\}} \tag{7c}$$

where α is the loss factor and can be considered as another unknown variable. Equation (7) can be written in a matrix format

$$\begin{bmatrix} 1 & 0 & 0 \\ 0 & -e^{-2\gamma\Delta d^{(0)}} & \left(\mathbf{\Gamma}_{\text{meas}}^{\text{chamber}} - \mathbf{\Gamma}_{\text{meas}}^{\text{offset}(0)}\right) e^{-2\gamma\Delta d^{(0)}} \\ \vdots & \vdots & \vdots \\ 0 & -e^{-2\gamma\Delta d^{(n)}} & \left(\mathbf{\Gamma}_{\text{meas}}^{\text{chamber}} - \mathbf{\Gamma}_{\text{meas}}^{\text{offset}(n)}\right) e^{-2\gamma\Delta d^{(n)}} \end{bmatrix} \cdot \begin{bmatrix} \mathbf{e}_1 \\ \mathbf{e}_2 \\ \mathbf{e}_3 \end{bmatrix} = \begin{bmatrix} \mathbf{\Gamma}_{\text{meas}}^{\text{chamber}} \\ \mathbf{\Gamma}_{\text{meas}}^{\text{offset}(0)} - \mathbf{\Gamma}_{\text{meas}}^{\text{chamber}} \\ \vdots \\ \mathbf{\Gamma}_{\text{meas}}^{\text{offset}(n)} - \mathbf{\Gamma}_{\text{meas}}^{\text{chamber}} \end{bmatrix} \tag{8}$$

where $\mathbf{\Gamma} = \alpha + j\beta$ represents the complex propagation constant. For simplicity, we denote the short condition as the zero-offset position in (8). The three error terms ($\mathbf{e}_1$, $\mathbf{e}_2$, and $\mathbf{e}_3$)

TABLE I
ERROR TERMS AND MEASURED REFLECTION AT 18 GHz

	$\mathbf{e}_1$	$\mathbf{e}_2$	$\mathbf{e}_3$[a]	$\mathbf{\Gamma}_{\text{meas}}$
Value	$0.0420 - j0.0153$	$-0.0167 + j0.0674$	$0.0014 - j0.0235$	$0.0418 - j0.0150$[b]
Type-A uncertainty	$1.4 \cdot 10^{-4} + j1.4 \cdot 10^{-4}$	$1.5 \cdot 10^{-4} + j2.7 \cdot 10^{-4}$	$0.0020 + j0.0019$	0[c]
Type-B uncertainty	$0.0001 + j0.0001$	$0.0001 + j0.0001$	$0.0001 + j0.0001$	$0.0001 + j0.0001$

[a] Uncertainty in $\mathbf{e}_3$ makes negligible contributions to $u_{|\mathbf{\Gamma}_o|}$.
[b] Cart at 224.93 cm.
[c] $\mathbf{\Gamma}_{\text{meas}}$ measured once at each position, no random noise error.

can be solved linearly by first setting no loss ($\alpha = 0$) as an approximation. Next, the solved error terms along with $\alpha = 0$ are used as starting values to feed a full nonlinear least squares fit. In the nonlinear fit, all measurements of the offset short contribute equally; that is, the fitting weights for a series of (7c) are set to 1.

In practice, the fitted value $\mathbf{e}_1$ often differs from $\mathbf{\Gamma}_{\text{meas}}^{\text{chamber}}$. This may seem unsettling from the beginning. However, we have consistently observed the existence of standing-wave effects when the cart was translated under the empty-chamber condition. The small, yet discernible, ripple size revealed non-negligible reflections from the cart. Thus, the direct assignment of $\mathbf{\Gamma}_{\text{meas}}^{\text{chamber}}$ to $\mathbf{e}_1$ may introduce some errors in the calibration. The extraction of $\mathbf{e}_1$ must rely on the nonlinear fit from a set of offset measurements.

C. Uncertainty Analysis

Equation (3) indicates that the errors in eight variables (real and imaginary parts of $\mathbf{e}_1$, $\mathbf{e}_2$, $\mathbf{e}_3$, and $\mathbf{\Gamma}_{\text{meas}}$) contribute to the uncertainty of the target reflection coefficient ($\mathbf{\Gamma}_o$). The magnitude of $\mathbf{\Gamma}_o$ is often more of interest than its complex value. The uncertainty of $|\mathbf{\Gamma}_o|$ can be expressed as

$$u_{|\mathbf{\Gamma}_o|} = \sqrt{\sum_{m,n=1}^{8} \frac{\partial|\mathbf{\Gamma}_o|}{\partial x_m}\frac{\partial|\mathbf{\Gamma}_o|}{\partial x_n}\rho_{mn}u_{x_m}u_{x_n}}. \tag{9}$$

Here, $x_{m,n} = \Re$ or $\Im$ ($\mathbf{e}_1$, $\mathbf{e}_2$, $\mathbf{e}_3$, or $\mathbf{\Gamma}_{\text{meas}}$), and ρ_{mn} is the correlation coefficient.

There are type-A and type-B uncertainties contributing to each uncertainty term [18]. The type-A uncertainty comes from the least squares fit, corresponding to random noise in the experiment, and the type-B uncertainty represents the limitation of the instrument accuracy. Correlation in type-A uncertainties can be derived directly from the covariance matrix obtained from the numerical fit. Correlations in type-B uncertainties are somewhat tricky. To safely quote the measurement uncertainty, we compute both scenarios, i.e., fully correlated and fully uncorrelated for the cross terms, and take the larger of the two.

The full expansion of the derivative factors in (9) is unenlightening and is omitted here. We also want to point out that the second term in the denominator in (3) can be safely neglected during the uncertainty computation to simplify the calculation. Such an approximation shows very good accuracy for objects of small reflection ($|\mathbf{\Gamma}_o| < 0.03$), which applies to the calibration targets. The number of error terms is then reduced to six, and their derivative terms are given by

$$\frac{\partial|\mathbf{\Gamma}_o|}{\partial\Re(\mathbf{e}_1)} = \frac{\Re(\mathbf{e}_1) - \Re(\mathbf{\Gamma}_{\text{meas}})}{|\mathbf{\Gamma}_o||\mathbf{e}_2|^2} \tag{10a}$$

$$\frac{\partial|\mathbf{\Gamma}_o|}{\partial\Im(\mathbf{e}_1)} = \frac{\Im(\mathbf{e}_1) - \Im(\mathbf{\Gamma}_{\text{meas}})}{|\mathbf{\Gamma}_o||\mathbf{e}_2|^2} \tag{10b}$$

$$\frac{\partial|\mathbf{\Gamma}_o|}{\partial\Re(\mathbf{e}_2)} = \frac{-|\mathbf{\Gamma}_o|\Re(\mathbf{e}_2)}{|\mathbf{e}_2|^2} \tag{10c}$$

$$\frac{\partial|\mathbf{\Gamma}_o|}{\partial\Im(\mathbf{e}_2)} = \frac{-|\mathbf{\Gamma}_o|\Im(\mathbf{e}_2)}{|\mathbf{e}_2|^2} \tag{10d}$$

$$\frac{\partial|\mathbf{\Gamma}_o|}{\partial\Re(\mathbf{\Gamma}_{\text{meas}})} = \frac{\Re(\mathbf{\Gamma}_{\text{meas}}) - \Re(\mathbf{e}_1)}{|\mathbf{\Gamma}_o||\mathbf{e}_2|^2} \tag{10e}$$

$$\frac{\partial|\mathbf{\Gamma}_o|}{\partial\Im(\mathbf{\Gamma}_{\text{meas}})} = \frac{\Im(\mathbf{\Gamma}_{\text{meas}}) - \Im(\mathbf{e}_1)}{|\mathbf{\Gamma}_o||\mathbf{e}_2|^2}. \tag{10f}$$

Some sampled values of $\mathbf{e}_1$, $\mathbf{e}_2$, $\mathbf{e}_3$, and $\mathbf{\Gamma}_{\text{meas}}$ along with their associated uncertainties at 18 GHz are listed in Table I. Although the type-A uncertainty of $\mathbf{e}_3$ is about one order of magnitude higher than the others, its contribution diminishes significantly in the error propagation due to its small derivative factors in (9), as we mentioned earlier. A full uncertainty calculation to include the contributions of $\mathbf{e}_3$ reveals no difference neglecting them in our test program. The choice of type-B uncertainty will be addressed in Section V.

D. Free-Space Calibration Verification

Verification by measuring a mismatched airline is a popular way to validate the calibration in coaxial and waveguide measurements. An equivalent counterpart can be realized by a dielectric slab in free-space measurements, as shown in Fig. 3. The total reflection due to the multiple reflections on the air and dielectric interfaces can be expressed as follows:

$$\begin{aligned}\mathbf{\Gamma}_{\text{total}} &= \mathbf{\Gamma}_{ij} + \mathbf{T}_{ij}\mathbf{\Gamma}_{ji}\mathbf{T}_{ji}\exp(-\boldsymbol{\gamma}\cdot 2\Delta d) \\ &\quad + \mathbf{T}_{ij}\mathbf{\Gamma}_{ji}^3\mathbf{T}_{ji}\exp(-\boldsymbol{\gamma}\cdot 4\Delta d) + \cdots \\ &= \mathbf{\Gamma}_{ij} + \frac{\mathbf{T}_{ij}\mathbf{\Gamma}_{ji}\mathbf{T}_{ji}\exp(-\boldsymbol{\gamma}\cdot 2\Delta d)}{1 - \mathbf{\Gamma}_{ji}^2\exp(-\boldsymbol{\gamma}\cdot 2\Delta d)}.\end{aligned} \tag{11}$$

Here, $\mathbf{\Gamma}_{ij}$ and $\mathbf{T}_{ij}$ represent the reflection and the transmission coefficients at the interface ij. More specifically, they are

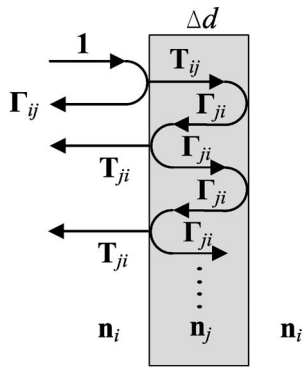

Fig. 3. Multipath reflections of a normal incidence radiation on a dielectric slab (n_j) in medium (n_i).

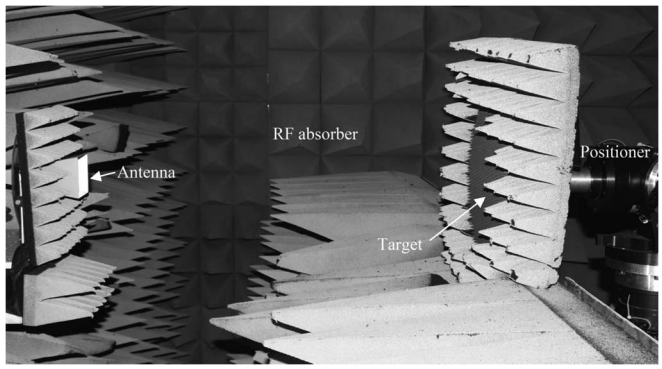

Fig. 4. Setup of measurements in the anechoic chamber.

related to the refractive index of the materials in the following equations:

$$\Gamma_{ij} = \frac{n_i - n_j}{n_i + n_j} \tag{12a}$$

$$\mathbf{T}_{ij} = \frac{2n_i}{n_i + n_j}. \tag{12b}$$

We note that the multiple reflection effects are modeled under the normal-incidence condition. Radiation from the transmitting antenna produces approximately normal incidence with a uniform phase in the far-field region, which validates the assumption of the model. In the near field, the radiation presents a spherical wavefront with nonuniform phase on the objects. In order to model this effect accurately, the incoming wave needs to be divided into a number of segments with corresponding incidence angle and phase delay. The total reflection is the superposition of all reflection components. To simplify the verification process, we kept the distance between the dielectric slab and the horn antenna much greater than the far field distance ($2D^2/\lambda$, where D is the length of the longer side of the antenna aperture and λ is the wavelength of the radiation) in the experiment. Therefore, the de-embedded reflection coefficients from dielectric slab measurements provide a legitimate comparison against the theoretical computation based on the model using (11) (see results in Section IV).

III. Experimental Setup

We measured the reflection coefficient from a blackbody target at an increment of 0.2 GHz in the range from 18 to 26 GHz. In addition to the calibration target, we also measured the empty-chamber condition and the reflections from a flat metal plate and a piece of dielectric slab, both cut to a size matching the shape of the calibration target. We used two types of antennas: a pyramidal standard-gain horn with an aperture of 10.16 cm $\times$ 8.26 cm and a full-width at half-maximum (FWHM) of approximately 12° and a conical horn with an aperture of 5.72 cm in diameter and an FWHM of approximately 14°, connected separately to a commercial VNA in different experiments. The VNA was calibrated at the input flange to the antenna with the open-short-load calibration method, and all measured reflection coefficients are with respect to this reference plane. The measurements were performed in the NIST anechoic chamber with a size of 5 m $\times$ 5 m $\times$ 8 m, which has been well characterized for use in the 400 MHz–40 GHz frequency range [19]. In a separate characterization, we measured the reflectivity of some RF absorbers, the same material used for chamber wall coverage. The magnitude of the reflection coefficients was about 0.002 for the lower half of the 18–26-GHz frequency band and about 0.004 for the upper half. Although the chamber is imperfect in practice, the nonlinear fitting using (7) will correct the imperfection to produce the correct $\mathbf{e}_1$ as we stated in Section II-B.

A photograph with the antenna and the target setup in the anechoic chamber is shown in Fig. 4. All the objects were mounted on a precise positioner that operates over a longitudinal range of approximately 5 m. The rails and all metallic parts of the cart are covered with an RF absorber. Although the minimum separation distance between the antenna and all objects (target, metal plate, and dielectric slab) was different, the moving ranges of the cart position were kept the same for all objects. We recorded the minimum separation distance measured by a laser range finder as a reference to correct the offset. For the calibration target, the minimum distance was 30.4 cm; for the metal plate, it was 38 cm, representing the offset distances as opposed to the cart positions. Measurements were made for two different ranges of separation distances between the antenna and the target, with a step size of 0.5 mm. The two ranges corresponded to the cart position from 0 to 10 cm and from 225 to 235 cm. The calibration target was a circular disc with a diameter of 330 mm, lent by a group at the National Aeronautics and Space Administration Goddard Space Flight Center. The target consisted of an iron-loaded epoxy coating on a machined aluminum tetrahedral pyramidal substrate. Most measurements were performed with the calibration target at ambient temperature (nominally 296 K). We also measured the reflection coefficients of the target heated to approximately 350 K to simulate the condition in its real applications. The physical temperature was measured by calibrated platinum resistance thermometers embedded in the target back side, showing a temperature of 349.7 $\pm$ 0.7 K during experiments.

IV. Measurement Results

Fig. 5 shows the measured data of the flat plate and the target at a typical frequency (18 GHz) in the range of separation

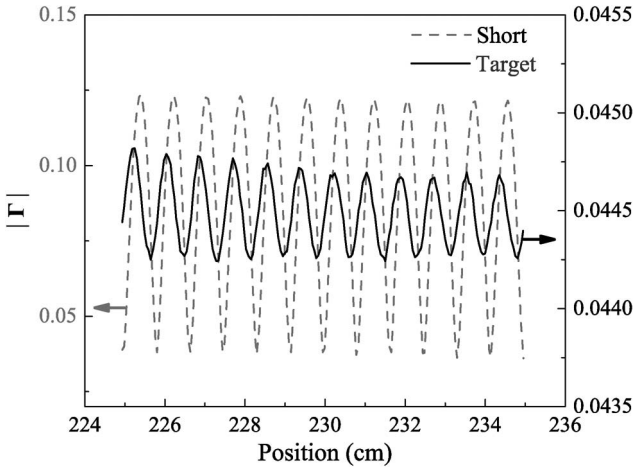

Fig. 5. Raw measurements of (gray dashed line) the flat plate and (black solid line) the target at 18 GHz. The ripple size of the flat plate is more than two orders of magnitude higher than that of the target.

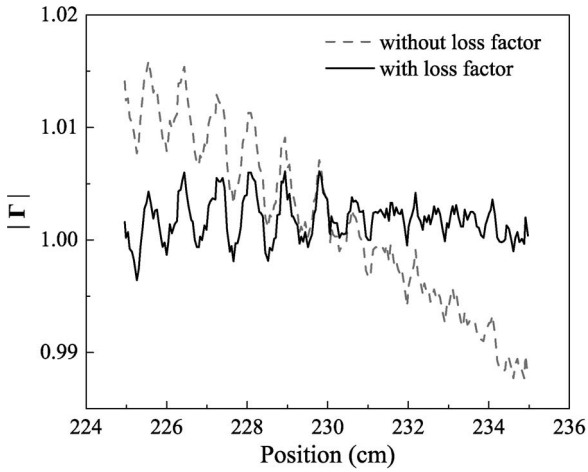

Fig. 7. Corrected magnitude of reflection coefficient of the flat metal plate in the 225–235-cm range at 18 GHz from (gray dashed line) calibration with no loss factor and (black line) calibration with loss factor.

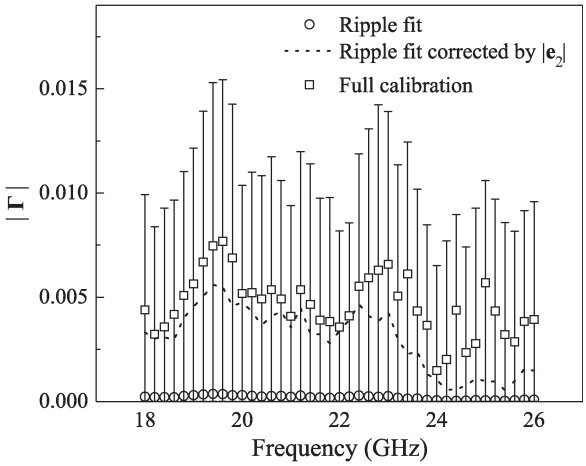

Fig. 6. Corrected magnitude of reflection coefficient of the target as a function of frequency calculated from different methods.

distances. Both plots indicate the standing wave effects with the ripple size dependent on the reflection characteristic of the objects. Qualitatively speaking, measurements of an object of high reflection at measured frequencies result in a large ripple, and vice versa. The ripple size of the flat metal plate is seen to be larger by more than two orders of magnitude than that of the target. The ripple size of the target at most of the measured frequencies is below 0.0005, much smaller than the uncertainty of the commercial VNA. Fig. 6 represents the corrected reflection coefficients in magnitude of the target from different methods. The ripple method represents the product of $\mathbf{e}_2$ and $\mathbf{\Gamma}$, showing roughly one order of magnitude lower than the true value of $\mathbf{\Gamma}$. The reflection of the target is greatly underestimated by using the ripple method. The full calibration method provides the most accurate way to determine the reflection coefficient of the target. We also noticed that an approximation can be made from a simple division of the value from the ripple method and the error term $\mathbf{e}_2$ solved from the full calibration, showing a reasonably close agreement to the full calibration method. The difference between the two is mainly due to the absence of the loss factor in the division method, which tends to underestimate the value. Since the target reflection was measured in a range of positions, we were able to obtain the corrected reflection at each position, providing a check for the measurement repeatability. The value presented in the figure at each frequency for the full calibration is actually the average of the corrected values for all positions, and the error bars correspond to a combination of the uncertainty based on Section II-C and the maximum and the minimum values calculated from all positions. The blackbody target exhibits low reflective properties with its reflection coefficient below 0.008, corresponding to a -40-dB reflectance, in the range of measured frequencies. The heated target exhibited almost no change of reflection, and the difference is well below the uncertainty.

As mentioned in Section II, the loss factor α is a crucial parameter in the de-embedding process. It is confirmed by checking the corrected reflection coefficients of the flat metal plate by using solved error terms $\mathbf{e}_{1,2,3}$ and α. If we perform the calibration in the absence of the loss term α, the corrected reflection coefficient shows a descending trend as the distance increases (shown as the gray dashed line in Fig. 7). The descending trend reflects the reduced radiation incident on the object when it moves away from the antenna. With the loss factor considered, the calibration corrects the error and balances the line (shown as the black line in Fig. 7) around its calibrated value, nominally 1, in the entire range. The error is correspondingly reduced by a factor of 3 from about ± 0.015 to ± 0.005.

Plots of uncertainty as a function of frequency are shown in Fig. 8. The value of $u_{|\mathbf{\Gamma}_o|}$ is computed by (9) from uncertainty contributions of $\Re$ and $\Im$ ($\mathbf{e}_{1,2}$ and $\mathbf{\Gamma}_{\mathrm{meas}}$). The contributions from $\mathbf{e}_3$ are omitted here as mentioned in Section II-C. The fully uncorrelated uncertainty of $u_{|\mathbf{\Gamma}_o|}$ is larger than its fully correlated uncertainty. The fully uncorrelated values are chosen in combination with the value range at all positions to specify the error bars in the final report. Although $u_{|\mathbf{e}_2|}$ appears larger than the other two in Fig. 8, $u_{\mathbf{e}_1}$ and $u_{\mathbf{\Gamma}_{\mathrm{meas}}}$ actually dominate due to their stronger preceding derivative factors.

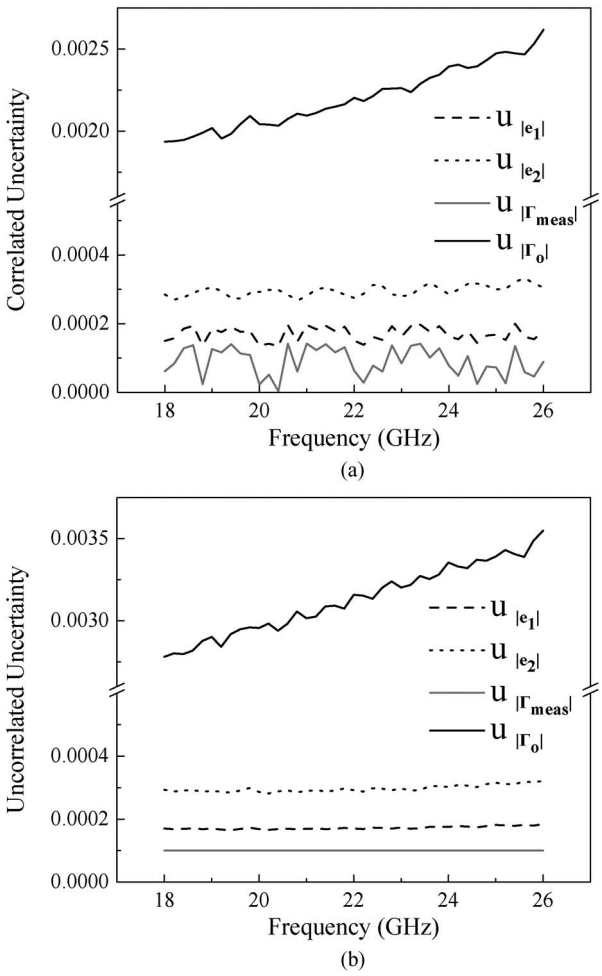

Fig. 8. Uncertainty values $u_{|\mathbf{e}_1|}$, $u_{|\mathbf{e}_2|}$, $u_{|\mathbf{\Gamma}_{\mathrm{meas}}|}$, and $u_{|\mathbf{\Gamma}_o|}$ as a function of frequency. (a) Correlated case. (b) Uncorrelated case.

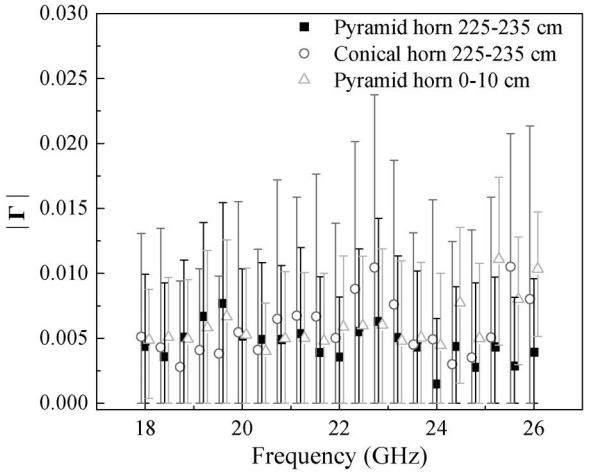

Fig. 9. Calibrated magnitude of reflection coefficients of the target as a function of frequency by the use of different antennas and in different measurement ranges.

Measurements with different antennas and in different position ranges were used to validate the calibration method. Fig. 9 shows the calibration results from three different conditions: objects in 225–235 cm with the pyramidal horn and the conical horn and objects in 0–10 cm with the pyramidal horn. The results agree well for most of the frequencies except for a couple of frequencies at the high end of the frequency band for measurements in the 0–10-cm range. Generally, the near-field measurements present a great amount of complexity and difficulty. Although the inclusion of the loss factor helps correct the effects, the error associated with the loss factor shows a higher standard deviation (available from the nonlinear data fitting) at higher frequencies than at lower frequencies. Therefore, the occurrence of the discrepancy at high frequencies in near-field measurements is reasonable. This also suggests that a more comprehensive model related to the specific radiation pattern, rather than a simple exponential function, would help improve the calibration, particularly in the near-field range. Furthermore, it is noteworthy that the error bars for the measurements using the conical horn are mostly larger than those from the pyramidal horn. The larger error is mainly due to less signal gain produced by the conical horn, which, in turn, introduced more noise to the measurement data. Aside from the validation of the calibration algorithm, Fig. 9 also guides the optimization of the measurement setup. To better measure the low reflection target, we should choose a high-gain antenna and carry out the measurements in the midfield or far field.

The calibration accuracy was further checked by de-embedding reflection coefficients from the far-field measurements on a dielectric slab made of 1422 cross-linked polystyrene. Such material has been a standard reference for material characterization due to its excellent uniformity and manufacture repeatability, as well as nearly constant EM properties over a broad frequency band [20]. We measured the free-standing polystyrene slab with no components on its back. In other words, EM radiation can propagate through the slab to the back wall of the anechoic chamber. The polystyrene slab had a thickness of 12.94 mm. Its relative permittivity and loss tangent are 2.55 and 0.0006, respectively. Theoretical calculation was made based on these values and used as a reference for checking the experimental results. Fig. 10 shows very good agreement between the experiments and theory for both values of magnitude and phase. The error bars of the magnitude values were calculated from the full uncertainty analysis, including both type-A and type-B uncertainties, whereas the error bars of the phase values simply represent the range of the de-embedded values at various measured positions. We did not exercise extra efforts for a full uncertainty analysis of the phase value since the phase information is considered to be of less interest for current blackbody target reflection study. The main purpose here is to demonstrate how well the experiments match the theoretical prediction. As we expected, the phase error greatly expands when the phase value is close to $\pm 180^\circ$ or the magnitude of the complex value is close to zero.

V. Discussion and Conclusion

The low reflection from the blackbody calibration target made the measurements and the de-embedding very challenging. The measured standing-wave ripple size (mostly < 0.0005) from the target reflection in the midfield range was much lower than the manufacturer's specifications for the VNA uncertainty, which is about 0.001 in the frequency range of the

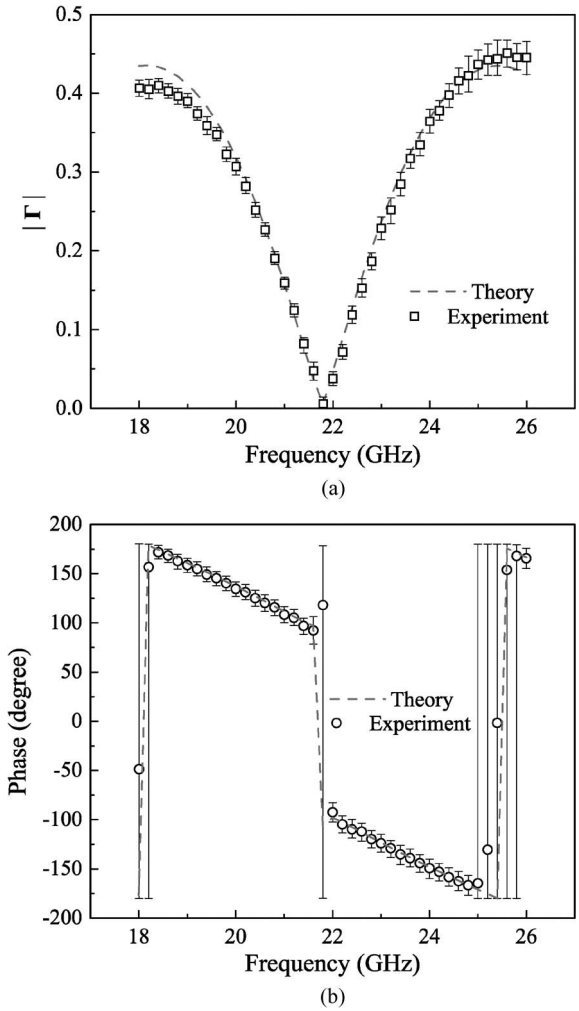

Fig. 10. De-embedded complex reflection coefficients of a 12.94-mm-thick polystyrene sheet ($\epsilon_r = 2.55$ and $\tan\delta = 0.0006$) in comparison with the theoretical values: (a) Magnitude and (b) phase angle.

measurements. However, the ± 0.001 is the total uncertainty, including both correlated and uncorrelated errors, whereas we are interested only in the uncertainty in the size of the ripple, which includes no error contributions that are correlated from point to point. We have insufficient information to determine the point-to-point uncertainty or the uncertainty in the ripple magnitude, so we made a rough estimate that the type-B uncertainty in the ripple is 0.0001, a very conservative guess that corresponds to more than 20% of the measured ripple size for most frequency points. The de-embedding of measurements in the near field seems less reliable and may require more sophisticated modeling for any specific combination of antenna and targets to account for the spherical wave front. However, the near-field measurements may be a better choice in terms of the uncertainty. The ripple size of the standing wave scales up in the near field due to much higher signal level, resulting in less measurement error.

Some systematic drifts of measured reflection coefficients, which may relate to the environmental temperature instability of the anechoic chamber, further aggravate the matter. A parallel investigation showed a temperature drift of more than 2 K in the anechoic chamber overnight. A great improvement of temperature stability in our measurement environment is currently limited owing to the presence of major reconstruction of the facility. Nevertheless, the experimental results prove our capability of characterizing low reflection microwave brightness standards by the use of current instrumentation and algorithms.

Aside from the VNA and environmental instability, the alignment of components is another possible error source. Our alignment capability was very limited previously, which led to difficulty with assessing the uncertainty due to misalignment. We have recently constructed a rigid platform for mounting waveguides and the horn antenna in a more controllable manner. The alignment accuracy was improved to about ± 20 arcsecond between the antenna axis and the target center. Among all error sources for $u_{\mathbf{e}_1}$ and $u_{\mathbf{\Gamma}_{\mathrm{meas}}}$, we estimate that the VNA systematic error dominates based on the fact that measurable signals (the ripple size) are below the specified instrument uncertainty. Furthermore, the observation of decreased error bar size in the close-range measurement confirmed our tentative conclusion.

We have specifically carried out the reflectivity study over the K-band (18–26.5 GHz) since we did intensive measurements of the brightness temperature in this band previously with our WR-42 waveguide radiometer. In principle, the calibration framework can be extended to other frequency ranges. The operating frequency range of our VNA instrument was 10 MHz to 67 GHz. However, the reliable operation range of the anechoic chamber limits the frequency to 0.4 to 40 GHz. In addition, the individual frequency band coverage becomes more and more limited for any waveguides larger than WR-90 (X-band; 8.2–12.4 GHz) when characterization at lower frequencies is of interest. On the other hand, the mechanical alignment of the components, including the horn antenna and the object, is expected to be more challenging due to the reduced size of the waveguide as the frequency increases.

In conclusion, we have developed and demonstrated a free-space calibration technique to extract the reflection coefficients of the brightness standard at microwave frequencies. The full calibration using known reflective components is needed to correct all the error terms, which allows us to solve for the unknown reflection from any object. The loss factor, accounting for the radiation pattern variation as a function of the separation distance between the antenna and the OUTs, is critical for the calibration accuracy. The developed calibration technique was validated by testing different measurement hardware and by checking measurements of a well-known polystyrene sample against the theory. The calibration target showed a close-to-blackbody property, with its power reflectivity below -40 dB at all measured frequencies.

ACKNOWLEDGMENT

The authors would like to thank D. Camell, R. Billinger, and D. LeGolvan at the National Institute of Standards and Technology, Boulder, for facilitating experiments in the anechoic chamber. The authors would also like to thank P. Racette at the National Aeronautics and Space Administration Goddard Space Flight Center for providing the calibration target.

REFERENCES

[1] E. G. Njoku and L. Li, "Retrieval of land surface parameters using passive microwave measurements at 6 to 18 GHz," *IEEE Trans. Geosci. Remote Sens.*, vol. 37, no. 1, pp. 79–93, Jan. 1999.

[2] L. A. Jones, J. S. Kimball, K. C. McDonald, S. T. K. Chan, E. G. Njoku, and W. C. Oechel, "Satellite microwave remote sensing of boreal and arctic soil temperatures from AMSR-E," *IEEE Trans. Geosci. Remote Sens.*, vol. 45, no. 7, pp. 2004–2018, Jul. 2007.

[3] C. Surussavadee and D. H. Staelin, "Global millimeter-wave precipitation retrievals trained with a cloud-resolving numerical weather prediction model, part I: Retrieval design," *IEEE Trans. Geosci. Remote Sens.*, vol. 46, no. 1, pp. 99–108, Jan. 2008.

[4] W. T. Crow, D. G. Miralles, and M. H. Cosh, "A quasi-global evaluation system for satellite-based surface soil moisture retrievals," *IEEE Trans. Geosci. Remote Sens.*, vol. 48, no. 6, pp. 2516–2527, Jun. 2010.

[5] D. Burrage, J. Wesson, and J. Miller, "Deriving sea surface salinity and density variations from satellite and aircraft microwave radiometer measurements: Application to coastal plumes using STARRS," *IEEE Trans. Geosci. Remote Sens.*, vol. 46, no. 3, pp. 765–785, Mar. 2008.

[6] C. Melsheimer and G. Heygster, "Improved retrieval of total water vapor over polar regions from AMSU-B microwave radiometer data," *IEEE Trans. Geosci. Remote Sens.*, vol. 46, no. 8, pp. 2307–2322, Aug. 2008.

[7] C. Muth, W. A. Webb, W. Atwood, and P. Lee, "Advanced technology microwave sounder on the national polar-orbiting operational environmental satellite system," in *Proc. IGARSS*, Jul. 2005, pp. 99–102.

[8] Z. Wang, J. Li, S. Zhang, and Y. Li, "Prelaunch calibration of microwave humidity sounder on China's FY-3A," *IEEE Geosci. Remote Sens. Lett.*, vol. 8, no. 1, pp. 29–33, Jan. 2011.

[9] V. Kangas, C. C. Lin, and M. Betto, "Precipitation imager instrument concepts for future LEO meteorological missions," in *Proc. MicroRad*, Mar. 2010, pp. 196–199.

[10] J. Randa, A. E. Cox, and D. K. Walker, "Proposed development of a national standard for microwave brightness temperature," in *Proc. IGARSS*, Aug. 2006, pp. 3979–3982.

[11] A. K. Fung and K. S. Chen, *Microwave Scattering and Emission Models for Users*. Norwood, MA: Artech House, 2010, pp. 6–7.

[12] J. Baker-Jarvis, M. D. Janezic, J. H. Grosvenor, and R. G. Geyer, "Transmission/reflection and short-circuit line methods for measuring permittivity and permeability," NIST, Boulder, CO, NIST Tech. Note TN1355-R, Dec. 1993.

[13] J. Baker-Jarvis, M. D. Janezic, P. D. Domich, and R. G. Geyer, "Analysis of an open-ended coaxial probe with lift-off for nondestructive testing," *IEEE Trans. Instrum. Meas.*, vol. 43, no. 5, pp. 711–718, Oct. 1994.

[14] D. K. Ghodgaonkar, V. V. Varadan, and V. K. Varadan, "A free-space method for measurement of dielectric constants and loss tangents at microwave frequencies," *IEEE Trans. Instrum. Meas.*, vol. 37, no. 3, pp. 789–793, Jun. 1989.

[15] J. A. Jargon and R. B. Marks, "Two-tier multiline TRL for calibration of low-cost network analyzers," in *Proc. ARFTG*, Nov. 1995, pp. 1–8.

[16] D. M. Pozar, *Microwavewave Engineering*, 3rd ed. Hoboken, NJ: Wiley, 2004, pp. 189–196.

[17] C. Y. Cheng, Q. Wang, D. Z. Xu, and Y. M. Chen, "Design and emissivity meterage of 3 mm microwave black body," in *Proc. ICMMT*, Apr. 2007, vol. 1, pp. 1–4.

[18] BIPM, JCGM 100:2008, *Evaluation of Measurement Data—Guide to the Expression of Uncertainty in Measurement*. [Online]. Available: http://www.bipm.org/en/publications/guides/gum.html

[19] D. A. Hill, M. Kanda, E. B. Larsen, G. H. Koepke, and R. D. Orr, "Generating standard reference electromagnetic fields in the NIST anechoic chamber, 0.2 to 40 GHz," NIST, Boulder, CO, NIST Tech. Note TN1335, Mar. 1990.

[20] M. D. Janezic, J. D. Splett, K. J. Coakley, R. F. Kaiser, and J. H. Grosvenor, "Relative permittivity and loss tangent measurement with the NIST 60 mm cylindrical cavity," in *NIST Special Publication 260-159*. Washington, DC: U.S. Gov. Printing Office, 2004.

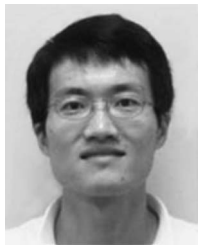

Dazhen Gu (S'01–M'08–SM'10) received the Ph.D. degree in electrical engineering from University of Massachusetts, Amherst, in 2007.

He has been with the Electromagnetics Division, National Institute of Standards and Technology, Boulder, CO, since November 2003. During the first three and a half years, he did his doctoral research in the development of terahertz imaging components and systems. In May 2007, he joined the Microwave Measurement Services project, where he has been involved in microwave metrology, particularly thermal noise measurements and instrumentation. His research interests include microfabrication, RF nanowire metrology, and calibration techniques for remote sensing.

Derek Houtz was born in Washington, DC, on September 5, 1989. He is currently working toward the B.S. degree in aerospace engineering and sciences at the University of Colorado, Boulder, and is expected to graduate in May 2011.

Since May 2009, he has been with the National Institute of Standards and Technology, Boulder. He works part time while school is in session and full time over the summers. He works through the university in a collaborative program called the Professional Research Experience Program.

James Randa (M'84–SM'91) received the Ph.D. degree in physics from the University of Illinois at Urbana–Champaign, Urbana, in 1974.

Since 1983, he has been with the Electromagnetics Division, National Institute of Standards and Technology (NIST), Boulder, CO. Until 1994, he worked on various topics in electromagnetic interference metrology. From 1994 to 2008, he worked on thermal noise metrology. He retired from NIST in 2008 and is now a Guest Researcher at NIST and a Senior Research Associate with the Department of Physics, University of Colorado, Boulder.

Dr. Randa has chaired the High-Frequency Working Group (GT-RF) of the Consultative Committee on Electricity and Magnetism since 2002.

David K. Walker (S'82–M'83–SM'07) received the B.A. degree in physics and mathematics from Hastings College, Hastings, NE, in 1980, and the B.S. and M.S. degrees in electrical engineering from Washington University, St. Louis, MO, in 1982 and 1983, respectively.

He spent eight years in industry working on microwave semiconductor device design and fabrication before joining the Electromagnetics Division, National Institute of Standards and Technology, Boulder, CO, in 1991. His work has included semiconductor fabrication, network analyzer calibration, and on-wafer measurements. He is the holder of five patents related to microwave technology. His current research interests include microwave thermal noise measurements, amplifier and transistor noise-parameter characterization, and calibration of microwave radiometers for remote sensing.